FISEVIER

Contents lists available at ScienceDirect

Applied Surface Science

journal homepage: www.elsevier.com/locate/apsusc



Full Length Article

Hydrogen bond interaction enhanced polymer electrolytes through functionalized nanosheets for high-stability lithium metal batteries

Lehao Liu, Tianrong Yang, Rubing Xu, Dingrong Long, Jiaxin Tu, Rongmin Zhou, Qian Zhao, Meicheng Li

State Key Laboratory of Alternate Electrical Power System with Renewable Energy Sources, School of New Energy, North China Electric Power University, Beijing 102206, China

ARTICLE INFO

Keywords: Polymer electrolyte Functionalized silica nanosheet Hydrogen bond interaction High ionic conductivity Lithium metal battery

ABSTRACT

Solid polymer electrolytes emerge as viable electrolyte candidates for lithium metal batteries (LMBs). Nevertheless, they face challenges of low ionic conductance, inadequate mechanical strength, and susceptibility to lithium dendrite generation. In this study, we address these challenges by incorporating porous silica nanosheets with functionalized groups (i.e., hydroxy, amino or carboxyl) in polyethylene oxide (PEO)-based electrolytes. Comprehensive characterizations and theoretical calculations disclose that these nanosheets effectively suppress PEO crystallization and promote lithium salt dissociation through hydrogen bonding between the polar groups of the nanosheets and the ether oxygen groups of PEO and the anions of lithium salts, respectively. Consequently, the functionalized nanosheet-modified electrolyte shows significant enhancement in ionic conductivity (8.9 \times 10^{-5} vs. 7.5×10^{-6} S cm $^{-1}$ at 30 °C) and mechanical toughness (1.47 vs. 0.61 MJ m $^{-3}$). The oxidization stability potential also increases from 3.95 V to 5.15 V. Furthermore, the modified electrolyte demonstrates superior dendrite suppression capability. Consequently, the cycling life of the Li||Li cells extends to 3000 h. The Li|| LiFePO4 cells also display exceptional electrochemical performance. This study gives a hydrogen bond design strategy for polymer electrolyte-based LMBs.

1. Introduction

Lithium-ion batteries are recognized for their exceptional characteristics, particularly their high energy density and absence of memory effects, which have facilitated their extensive applications in portable electronics, transportation, and other fields [1-4]. Nevertheless, operational safety limitations persist, including risks of electrolyte leakage and thermal decomposition under extreme conditions that may induce combustion incidents [5-7]. Replacing organic flammable liquid electrolytes with solid-state electrolytes offers a viable solution to address safety challenges. This approach also enables the use of lithium metal anodes for higher energy density [8-10]. Polyethylene oxide (PEO)based polymer electrolytes have garnered substantial research potential for their multifaceted advantages: cost-effectiveness in manufacturing processes, lightweight nature, superior film-forming characteristics, structural adaptability, and favorable interfacial adhesion with electrode components [11-13]. Despite these merits, technical barriers remain unresolved. The semi-crystalline structure of PEO matrices at ambient temperatures significantly impedes ion transport, yielding unsatisfactory ionic conductivity [14,15]. Additionally, these polymer electrolytes demonstrate suboptimal mechanical robustness and restricted high-voltage tolerance, with persistent challenges arising from continuous dendrite propagation through the soft electrolyte matrix, ultimately leading to lithium metal battery (LMB) failure via internal short-circuiting [16–18].

The introduction of inorganic or organic nanoscale additives into polymer matrices would elevate the ionic conductance of solid polymer electrolytes through dual mechanisms of crystalline phase suppression and lithium salt dissociation promotion [19–21]. Moreover, the incorporation of nanofillers can enhance their mechanical robustness and the capability to inhibit lithium dendrite growth [22–24]. Particularly noteworthy are two-dimensional (2D) nanostructured materials, which offer unique advantages stemming from their exceptional surface-to-volume ratios, high thermostability, and abundant surface functionalization sites [25–27]. However, the functions of 2D nanofillers are mostly ascribed to Lewis acid-base coordination and deep understanding of the

E-mail address: mcli@ncepu.edu.cn (M. Li).

^{*} Corresponding author.

complex interactions between 2D nanofillers and the other components in electrolytes is scarce [28]. Thus, related characterizations and theoretical simulations are needed to reveal the role and mechanism of 2D nanofillers in improving the electrolyte properties. It is also necessary to optimize the functional groups on 2D nanofillers to strengthen the nanofiller-polymer/lithium salt interactions for further improving the electrolyte properties.

Silica particles are abundant in earth and cost-effective, and their surficial functional groups are also easily tuned [29]. In this work, porous silica nanosheets (NSs) with three functionalized groups (i.e., hydroxy, amino or carboxyl) are incorporated in PEO-based electrolytes to boost the electrical, mechanical and electrochemical properties. Various experimental characterizations and theoretical calculations are also combined to disclose the role of the functional groups (Fig. 1). The hydrogen bonding between the polar groups of NSs and the ether oxygen groups of PEO chains can greatly disarrange PEO chains, thus elevating the chain segmental mobility and increasing the ionic conductivity. Besides, the hydrogen bond interaction between the polar groups and the anions of LiTFSI facilitates its decomposition for free Li⁺ cations, therefore further elevating the electrolyte's electrical performance. Furthermore, the mechanical robustness and electrochemical oxidization stability are greatly strengthened due to the hydrogen bond interactions. As expected, the functionalized NS-modified composite electrolyte (denoted as PL-NS) shows robust resistance against lithium dendrites, and the composite electrolyte-based LMBs possess excellent electrochemical performance.

2. Experimental section

2.1. Synthesis of functionalized porous silica nanosheets

The synthesis of functionalized porous silica nanosheets was performed by three steps (Fig. S1) (Supporting Information). Initially, 10 g of as-received vermiculite natural mineral (Sigma-Aldrich) after ball milling was dispersed into 1 L of saturated sodium chloride (NaCl) solution with agitating for 24 h at 110 °C. The solid phase was isolated and subsequently purified with water to remove residual NaCl by centrifugation. The sample obtained by centrifugation was placed into 1 L of 2 M lithium chloride (LiCl) solution with magnetic stirring at the same condition as Na $^+$ exchange process. The solid phase was isolated by centrifugation and rinsed six times in water to eliminate the excessive LiCl. The sample obtained by centrifugation was placed into 100 mL of HCl (36 wt%) with agitation for 12 h at 80 °C. The solid phase was isolated and then rinsed utilizing water until neutral pH. After repeating

the above process, the liquid supernatant was freeze-dried to obtain hydroxy-functionalized porous silica nanosheets (denoted as NSOs).

The functionalization of amino groups commenced with ultrasonic dispersion of NSOs (3 g) in toluene (100 mL), followed by the incorporation of triethylamine (5 mL) and aminopropyl triethoxysilane (APTES, 10 mL) and reflux for 24 h at 90 $^{\circ}\text{C}$. The synthesized product was centrifugated and then rinsed with anhydrous ethanol and water, respectively. The liquid supernatant was freeze-dried to get aminofunctionalized nanosheets (denoted as NSNs).

1 g of NSNs was dispersed in *N*, *N*-dimethylformamide (DMF, 100 mL), followed by the incorporation of maleic anhydride (1.2 g). The mixture was then refluxed at the same condition as that of NSN synthesis. After that, the mixture was centrifuged with solid phase collected and purified with DMF and water. Freeze-drying was employed to isolate the nanosheets and remove the residual solvent of the obtained solid phase. The carboxyl-functionalized nanosheets was named as NSCs

2.2. Preparation of PEO-LiTFSI-NS composite electrolytes

Nanosheets with mass of 0, 0.025, 0.078, 0.132 and 0.188 g were separately added in five bottles containing 5 mL of DMF. The mixtures were ultrasonicated for 1 h, and vigorously agitated for 24 h. Meanwhile, a solid mixture totaling 2.5 g of PEO ($M_{\rm w}=600,\!000$) and LiTFSI at an EO:Li $^+$ molar ratio of 18:1 was put in 31 mL of DMF and vigorously agitated for 24 h. The nanosheet/DMF solutions were subsequently combined with the polymer electrolyte solutions and agitated for 24 h. The resulting mixed solution were subject to solution cast into Teflon molds and thermally dried under vacuum for solvent evaporation. The PEO-LiTFSI-NS electrolytes with 0, 1, 3, 5 and 7 wt% silica nanosheets were denoted as PL, PL-NSX1, PL-NSX3, PL-NSX5 and PL-NSX7 (where X=0, N or C, represented as hydroxy, amino or carboxyl).

2.3. Material characterizations

Full descriptions of material characterizations including equipment specifications and operational parameters are provided in Text S1.

2.4. Density functional theory (DFT) calculations

DFT calculations were utilized to further uncover the interaction between the functionalized NSs and TFSI⁻. For a comprehensive description of the details, please refer to Text S2.

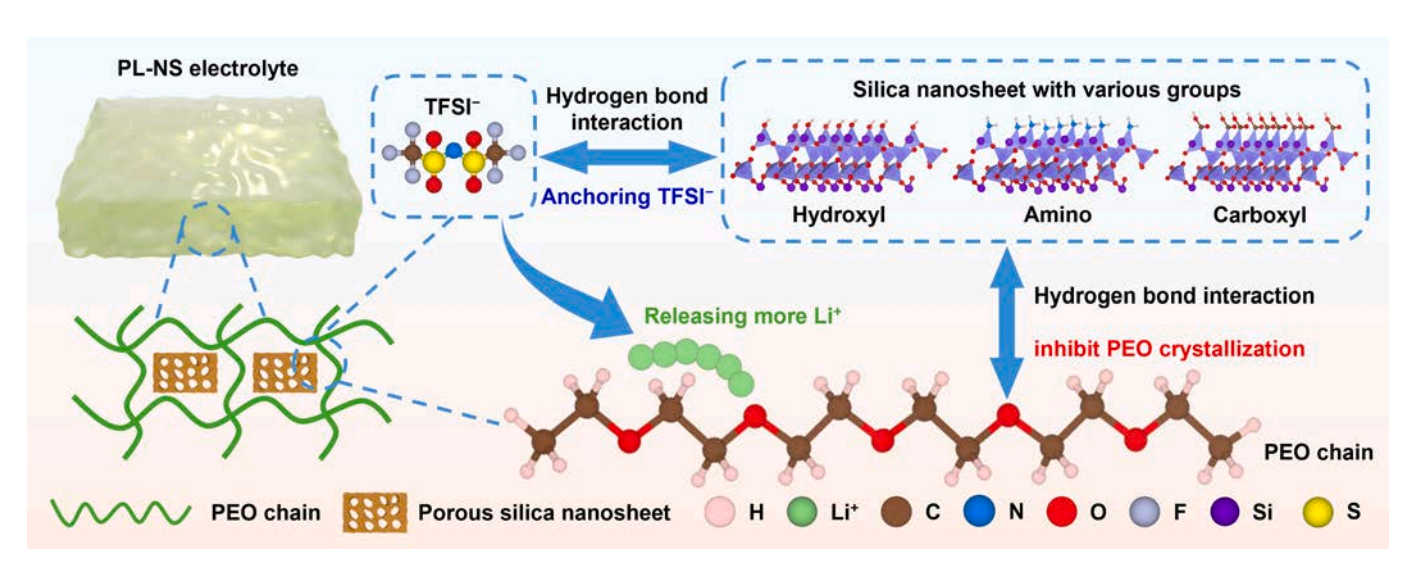


Fig. 1. Schematic illustration shows the role of functionalized porous silica nanosheets in composite polymer electrolyte of PL-NS.

2.5. Electrochemical measurements

Complete details of electrochemical measurements are documented in Text S3.

3. Results and discussion

3.1. Physicochemical characterizations of porous silica nanosheets

The vermiculite natural mineral shows a representative lamellar structure (Fig. 2a). The vermiculite natural mineral was then exfoliated by ion exchange and acid-treated to obtain the NSOs (Fig. S1) [30]. The NSOs possess an irregular nanosheet microstructure with abundant pores (Fig. 2b), which is attributed to the exfoliation by ion exchange and etching of magnesium octahedra.

To elucidate the textural characteristics of the vermiculite and the NSOs, nitrogen physisorption analysis was further performed. The resultant isotherms (Fig. 2c) reveal distinct adsorption behaviors between the two materials. Notably, the NSOs show overlapping adsorption–desorption branches with quasi-linear progression at low relative pressures ($P/P_0 = 0.05 - 0.45$), characteristic of microporous lamellar

architectures [27]. A pronounced type IV isotherm signature emerges in the elevated pressure regime (P/P $_0$ = 0.45 – 0.85), accompanied by an H3-type hysteresis loop diagnostic of mesoporous structures. In contrast, the vermiculite exhibits a type II isotherm profile, consistent with nonporous materials. Compared to the parent vermiculite (32.7 m 2 g $^{-1}$), the NSOs have a larger surface area of 309.3 m 2 g $^{-1}$. The NSOs also display a broad mesoporous domain (2 – 20 nm) while the vermiculite particles have primarily sub-nanometer scale pores (0 – 1 nm) (Fig. 2c inset). The wide-range diffraction peaks in Fig. 2d and the weak diffraction ring in Fig. 2b also confirms that the variation from vermiculite to amorphous silica, which is identical with the surface area increase after the acid treatment.

The surficial modification of the porous silica nanosheets was systematically investigated through a combination of XRD, FTIR, TGA and DLS measurements. The XRD patterns (Fig. 2d) demonstrate that both the amino- and carboxyl-functionalized nanosheets (NSNs and NSCs) have the similar amorphous structure to the NSOs, suggesting the non-destructive nature of the surface modification protocols [31,32].

To verify the successful functionalization, FTIR characterizations were conducted (Fig. 2e). A wide absorption envelope at $3425~\text{cm}^{-1}$ and a distinct band at $1635~\text{cm}^{-1}$ in all the samples are related to

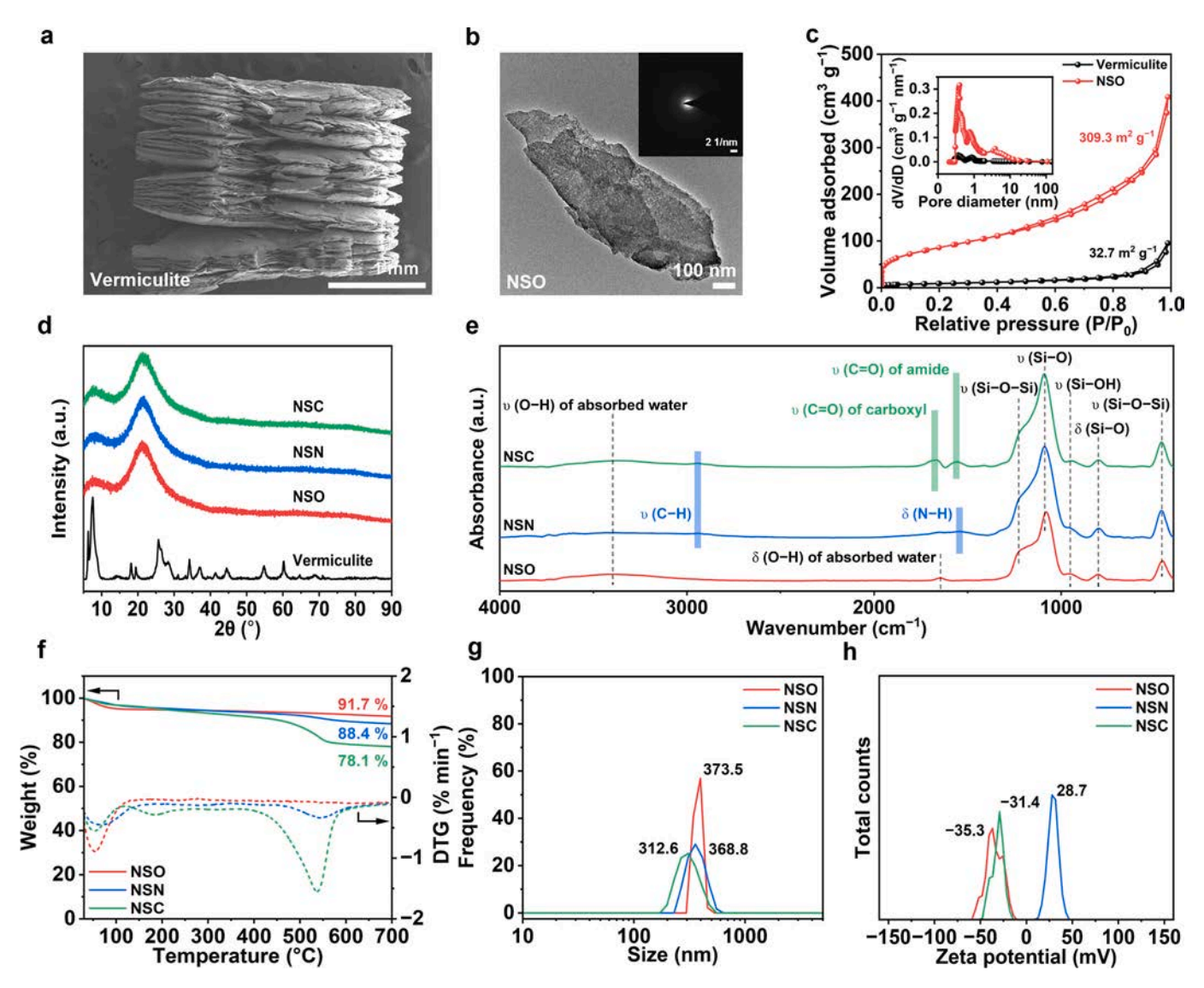


Fig. 2. Characterizations of functionalized porous silica nanosheets. (a) SEM image of vermiculite. (b) TEM image of NSOs (inset: corresponding SAED pattern). (c) Nitrogen adsorption—desorption isotherms of vermiculite and NSOs (inset: pore size distribution). (d) XRD patterns of vermiculite, NSOs, NSNs and NSCs. (e) FTIR spectra, (f) TGA curves, (g) size distribution and (h) zeta potential of NSOs, NSNs and NSCs.

physiosorbed water molecules within the porous architecture [29,33]. All the samples also have fundamental silica framework vibrations such as siloxane network vibrations (e.g., stretching of Si - O - Si and bending at 1200 and 453 cm $^{-1}$, Si - O stretching and bending at 1085 and 800 cm $^{-1}$), and surficial silanol vibrations (e.g., Si - OH stretching at 960 cm $^{-1}$) [29,30,33–35]. Besides, the NSNs display two absorption peaks at 1544 and 2941 cm $^{-1}$ corresponded to N - H bending and C - H asymmetric stretching vibrations, respectively, while the NSCs exhibit other peaks at 1570 and 1670 cm $^{-1}$ related to C=O stretching vibrations [32,36–40]. The FTIR and XRD results together demonstrate the successful surface modification from hydroxyl groups on the NSOs to amino groups on the NSNs and carboxyl groups on the NSCs while maintaining the pristine amorphous structure.

The TGA measurements were also taken to investigate the surface functionalization. As shown in Fig. 2f, all the samples had mass loss before 130 °C, due to the evaporation of residual solvent. The pristine NSOs had a weight loss of 8.3 % before 700 °C, because of the removal of residual solvent and the decomposition of hydroxyl groups [41]. The NSNs exhibited an abrupt weight decrement at 470 - 620 °C, ascribed to

the decomposition of APTES grafted on the NSN surface [42]. In comparison, the NSCs displayed three-stage thermal decomposition behavior: (1) initial gradual mass loss of $3.6\,\%$ at $30-130\,^{\circ}$ C, due to the residual solvent evaporation; (2) unobvious and linear weight reduction of $2.3\,\%$ at $130-240\,^{\circ}$ C, attributed to the decomposition of carboxylic groups [43]; (3) subsequent mass loss of $12.4\,\%$ at $390-600\,^{\circ}$ C arising from the thermal degradation of grafted APTES ligands and anhydride residues.

To better disclose the effect of the surface functionalization, DLS measurements were also performed (Fig. 2g-h). The average particle size decreased from 373.5 nm (of NSOs) to 368.8 nm (of NSNs) and 312.6 nm (of NSCs), while the zeta potential shifted from -35.3 mV (of NSOs) to 28.7 mV (of NSNs) and -31.4 mV (of NSCs), indicating the enhanced colloidal stability by the surficial functionalization. This would be beneficial for the even dispersion of the NSs in the polymer matrices.

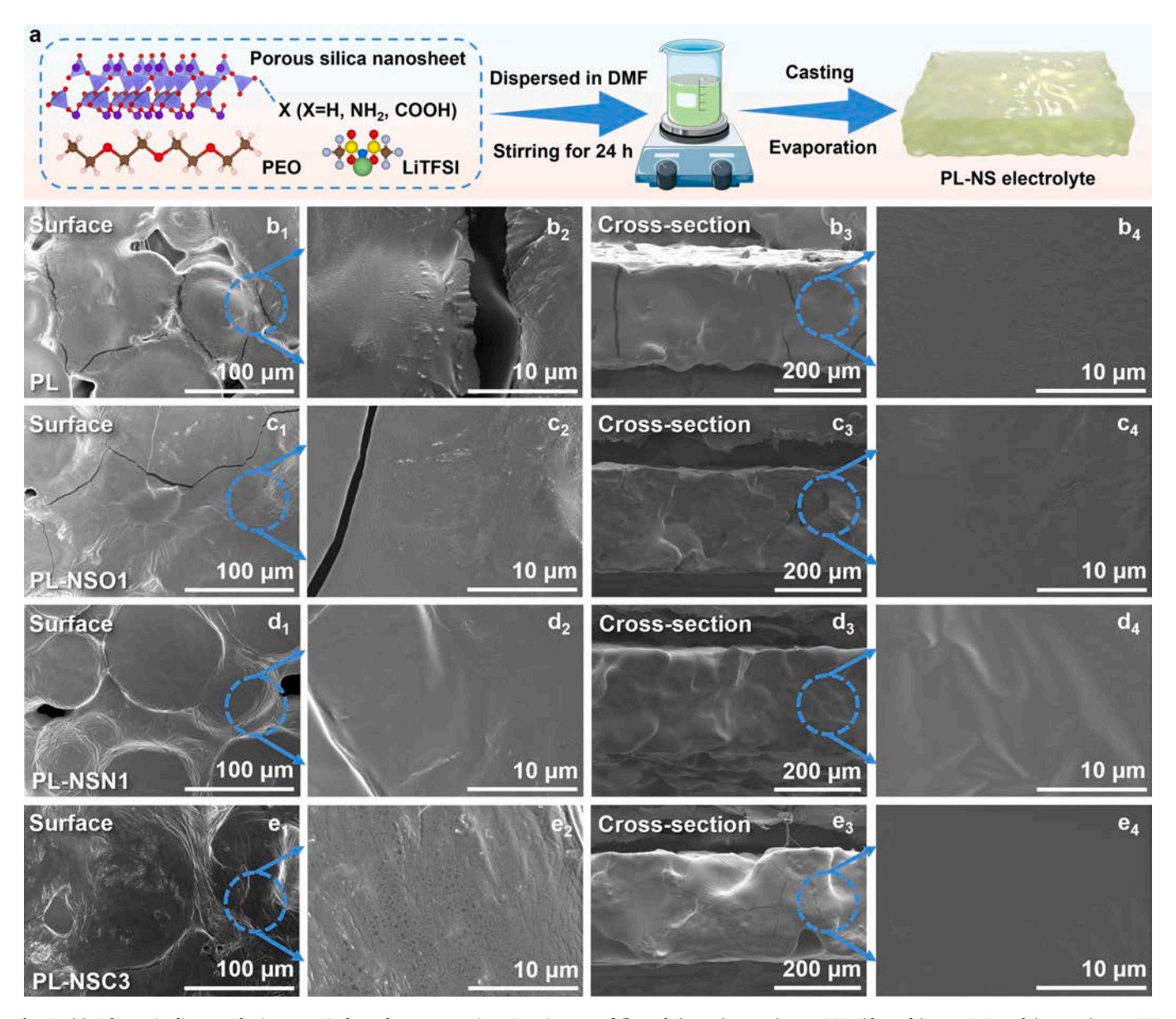


Fig. 3. (a) Schematic diagram depicts PL-NS electrolyte preparation. SEM images of (b_1-b_4) PL, (c_1-c_4) PL-NSO1, (d_1-d_4) PL-NSN1 and (e_1-e_4) PL-NSC3 electrolytes at $(b_1-b_2,\,c_1-c_2,\,d_1-d_2$ and $e_1-e_2)$ the surface and $(b_3-b_4,\,c_3-c_4,\,d_3-d_4$ and $e_3-e_4)$ the cross-section.

3.2. Morphology of electrolytes

The PEO-LiTFSI-NS electrolytes with various amounts of NSO, NSN and NSC were prepared using a facile solution casting method followed by vacuum drying (Fig. 3a), and their ionic conductivities at $30-80\,^{\circ}\mathrm{C}$ were also obtained (Fig. S2). According to the results, the proper filling amounts of NSO, NSN and NSC were 1, 1 and 3 wt%, respectively. Thus, the microstructure and properties of the PL, PL-NSO1, PL-NSN1 and PL-NSC3 electrolytes are discussed in the following parts.

Their morphology was examined by SEM (Fig. 3b - e). The thickness of the PEO-LiTFSI-NS electrolytes is $230-260~\mu m$. As illustrated in Fig. 3b - c, the PL and PL-NSO1 electrolytes have a coarse surface with apparent cracks and pores. In comparison, the PL-NSN1 and PL-NSC3 electrolytes have smooth surfaces and fewer cracks (Fig. 3d - e). This change should be related to the stronger hydrogen bonding interactions between the ether oxygen groups of PEO and the amino and carboxyl groups of the NSNs and NSCs, respectively, which is beneficial for elevating the densification (during the drying process) and mechanical robustness (See following Fig. 5b) of the composite electrolytes.

3.3. Ion transport mechanism of electrolytes

Ionic conductance is a significant electrical property for assessing the

practical applicability of electrolytes. The conductivities of the PL-NS electrolytes were investigated at 30 - 80 °C (Fig. 4a and Table S1). The pristine PL electrolyte exhibited a baseline conductivity of 7.5 \times $10^{-6}\,\mathrm{S\,cm^{-1}}$ at 30 °C. In comparison, the introduction of the NSs led to a substantial enhancement. The PL-NSO1, PL-NSN1 and PL-NSC3 electrolytes demonstrated significantly improved ionic conductivities of 6.7 \times 10^{-5} , 8.7 \times 10^{-5} and 8.9 \times $10^{-5}\,\mathrm{S}$ cm $^{-1}$, respectively. Further Arrhenius fitting analyses showed that the activation energy (E_a) progressively decreased from 1.05 eV (PL) to 0.76 eV (PL-NSO1), 0.74 eV (PL-NSN1) and 0.73 eV (PL-NSC3) (Fig. 4a). The reduction of the E_a value also indicated the critical role of the surficial functionalization on the NSs in lowering the ion transport energy barrier in the PEO-LiTFSI matrices [44].

A higher $\tau_{\text{Li+}}$ indicates a stronger migration propensity of lithium ions relative to anions [22]. As illustrated in Fig. S3, the $\tau_{\text{Li+}}$ values of the PL-NSO1, PL-NSN1, and PL-NSC3 electrolytes increase to 0.36, 0.39, and 0.39, respectively, demonstrating significant enhancement compared to the pristine PL electrolyte (0.17). The elevated $\tau_{\text{Li+}}$ is beneficial to suppressing spatial charge accumulation at electrodes, reducing electrochemical polarization during cycling, and mitigating lithium dendrite growth [25,45].

The reason why the incorporation of the NSs in the polymer matrices greatly enhanced Li⁺ transport kinetics was revealed. The FTIR spectra

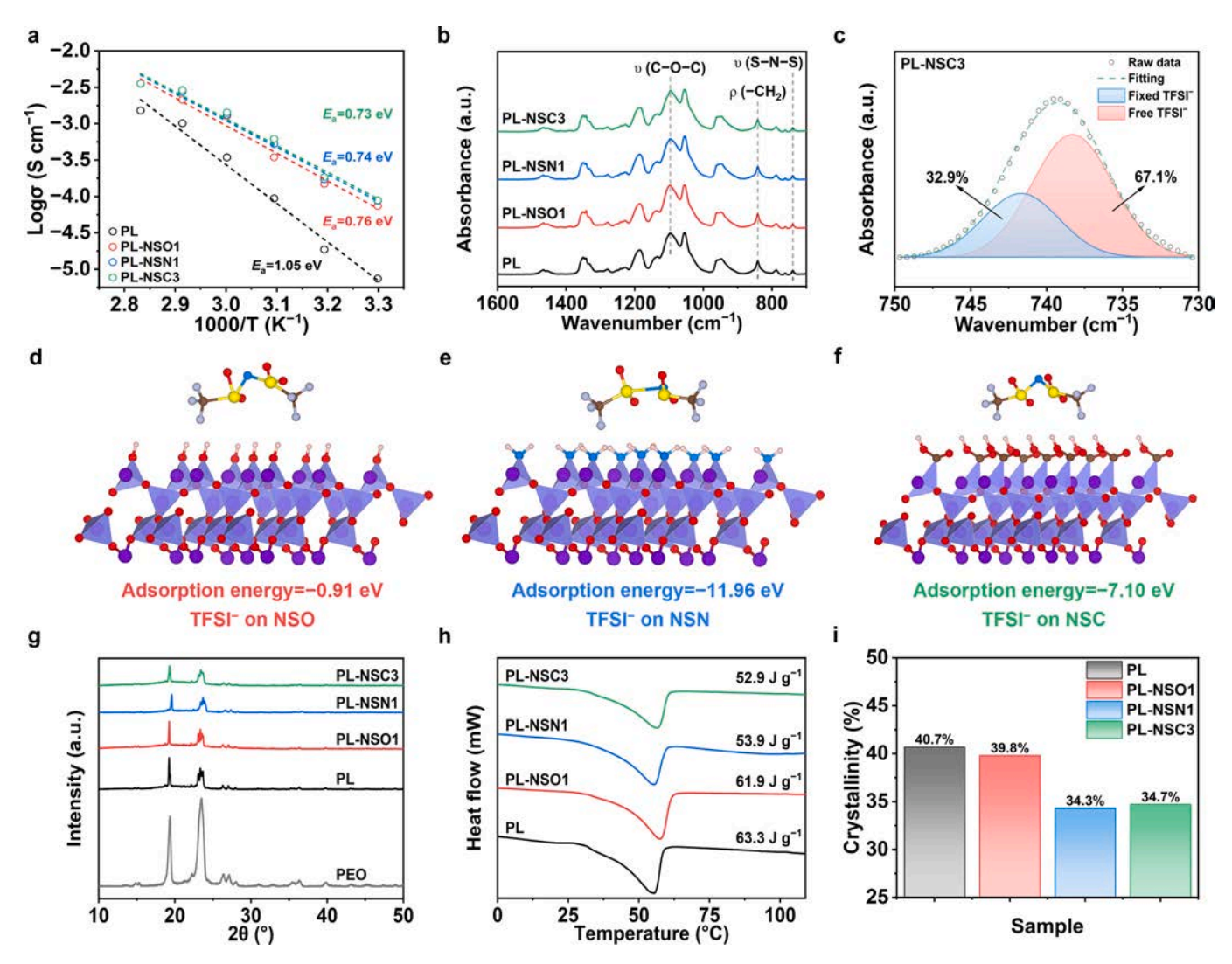


Fig. 4. Electrical properties. (a) Arrhenius plots and (b) FTIR spectra of electrolytes. (c) FTIR spectra of PL-NSC3 electrolyte fitted with Gaussian – Lorentzian ($R^2 = 0.99$). Optimized structures and corresponding E_{ads} of TFSI⁻ coordinated with (d) NSO, (e) NSN and (f) NSC. (g) XRD patterns of PEO and electrolytes. (h) DSC curves ranging from 0 to 110 °C and (i) corresponding calculated crystallinities of electrolytes.

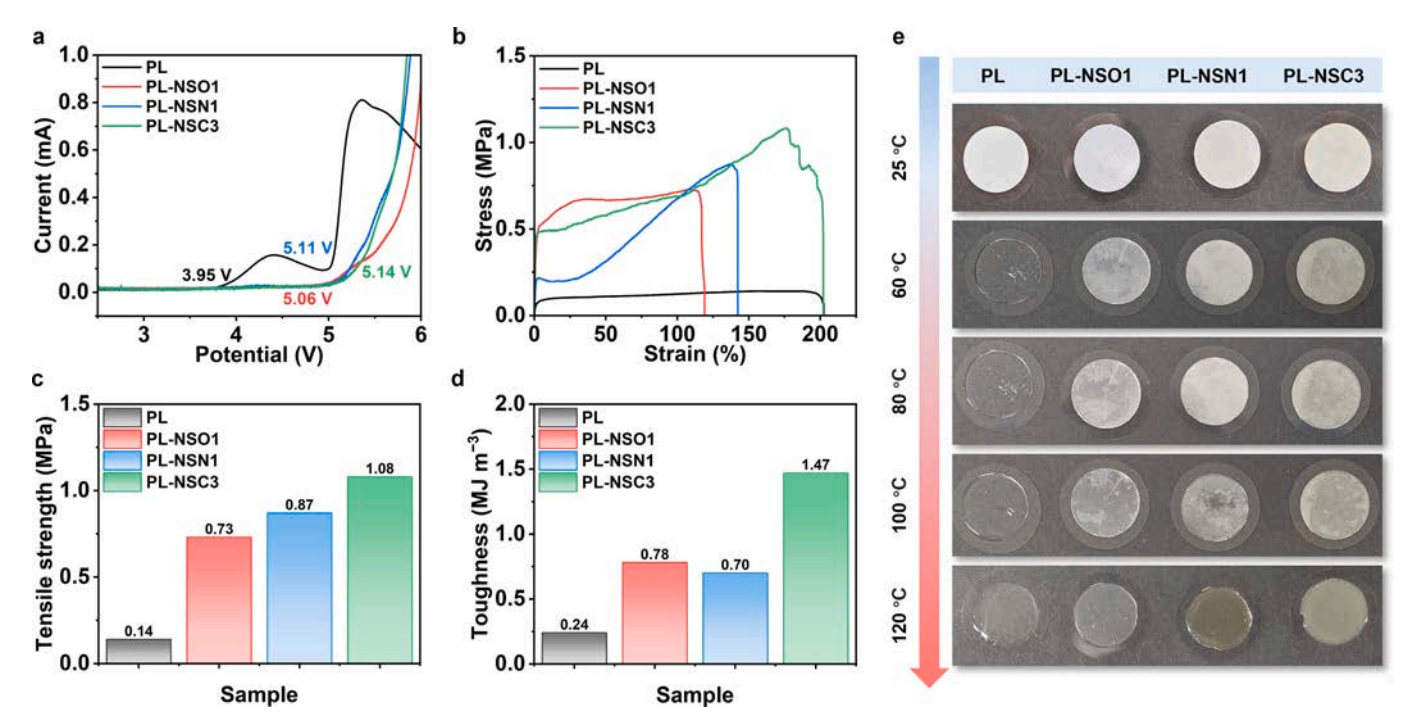


Fig. 5. Electrochemical stability and mechanical characteristics. (a) LSV curves, (b) tensile stress–strain curves, (c) tensile strength and (d) toughness of electrolytes. (e) Optical images of electrolyte discs heated to different temperatures and kept for 2 h.

(Fig. 4b) shows that there are no characteristic peaks of the NSs in the spectra of the electrolytes, indicating a sufficient coupling between the polymer matrices and the NSs during the fabrication process. The weakened absorbance peak near 1096 cm^{-1} in PL-NSN1 and PL-NSC3 electrolytes indicates hydrogen bonding between the functional groups on the NSs and the ether oxygen groups in PEO. This interaction would help to reduce PEO crystallinity and facilitate Li+ transport [16,46]. The FTIR absorbance peak related to symmetric stretching vibrations of S - N - S (\sim 740 cm⁻¹) was deconvoluted into two distinct peaks: one for the free $TFSI^-$ (738 cm^{-1}) and the other for the immobilized TFSI⁻ (742 cm⁻¹) [2,47]. Gaussian-Lorentzian fitting (Fig. 4c and S4) shows TFSI⁻ immobilization ratios of 13.1 %, 29.7 %, 31.3 %, and 32.9 % for the PL, PL-NSO1, PL-NSN1, and PL-NSC3 electrolytes, respectively. This analysis suggests that the NSs with the functional groups can anchor a substantial fraction of TFSI- anions, thereby releasing more free Li⁺ for ionic transport. Besides, the peak related to – CH2 vibrations of PEO is sensitive to the disintegration efficiency of lithium salts [48], and the decline of the peak intensity at $\sim 842 \, \mathrm{cm}^{-1}$ in the PL-NSN1 and PL-NSC3 electrolytes also implies the more free Li⁺ release due to the hydrogen bond interaction (Fig. 4b).

Further investigation into the interaction of functionalized NSs with TFSI $^-$ anions was conducted using DFT calculations. The optimized structures and corresponding adsorption energy ($E_{\rm ads}$) of TFSI $^-$ coordinated with the functionalized NSs (NSO, NSN and NSC) are given in Fig. 4d - f and Table S2. The NSNs ($-11.96~{\rm eV}$) and NSCs ($-7.10~{\rm eV}$) exhibit significantly lower $E_{\rm ads}$ values than the NSOs ($-0.91~{\rm eV}$). This indicates stronger hydrogen bonding between the functionalized NSNs and NSCs and TFSI $^-$. This also explains why the PL-NSN1 and PL-NSC3 electrolytes have much higher immobilization ratios of TFSI $^-$ (Fig. 4c and S4).

XRD and DSC measurements were then taken to reveal the role of the functionalized NSs. The XRD patterns show that the pristine PL electrolyte exhibited the peaks of PEO near 19° and 23° (Fig. 4g) [24]. In comparison, the peak intensity of the PL-NSO1, PL-NSN1 and PL-NSC3 electrolytes decreased greatly (especially PL-NSN1 and PL-NSC3), implying the lower PEO crystallinity and accelerated PEO chain movement in the composite electrolytes. Additionally, the DSC measurements

presented that the crystallinities of the PL and PL-NSO1 electrolytes were 40.7 % and 39.8 %, respectively (Fig. 4h - i). However, the PL-NSN1 and PL-NSC3 electrolytes had lower crystallinities of 34.3 % and 34.7 %, respectively, thus greatly improved the ionic transport along the amorphous PEO chains. The combination with the abovementioned characterization and simulation results indicated that the functionalized NSs demonstrate dual functionality in polymer electrolyte optimization, effectively inhibiting PEO crystallinity while simultaneously enhancing LiTFSI salt dissociation. This synergistic effect originates from distinct hydrogen bonding: (1) between the functional groups on the NSs and ether oxygen groups in PEO chains, and (2) interfacial coordination with TFSI $^-$ anions of lithium salt.

3.4. Electrochemical and mechanical properties of electrolytes

The high-voltage tolerance of the PL-NS electrolytes was assessed via LSV at 60 °C (Fig. 5a). The PL electrolyte exhibited an onset oxidation potential of 3.95 V. With the incorporation of the NSOs, the PL-NSO1 electrolytes demonstrated a broaden oxidation potential of 5.05 V. The further enhanced oxidation stability of the PL-NSN1 (5.11 V) and PL-NSC3 (5.14 V) electrolytes arises from the inhibited degradation of PEO and TFSI $^-$ at high voltages. This enhancement originates from the established strong hydrogen bond interactions as discussed in section 3.3.

The mechanical characteristics of the PL-NS electrolyte were characterized as well (Fig. 5b - d). The unmodified PL electrolyte had a tensile strength of 0.14 MPa. Conversely, the incorporation of the NSOs, NSNs and NSCs in the PEO-LiTFSI matrices resulted in enhanced tensile strengths of 0.73 (PL-NSO1), 0.87 (PL-NSN1) and 1.08 MPa (PL-NSC3). Moreover, the PL-NSO1 (0.78 MJ $\rm m^{-3}$), PL-NSN1 (0.70 MJ $\rm m^{-3}$) and PL-NSC3 (1.47 MJ $\rm m^{-3}$) electrolyte membranes exhibited higher toughness than the PL electrolyte membrane (0.24 MJ $\rm m^{-3}$), because of the hydrogen bonding between the functionalized NSs and the PEO matrix. The improved mechanical properties of the composite electrolytes would contribute to suppressing dendrite growth. Notably, the strength of the PL-NSC3 electrolyte exceeds the ~ 1 MPa threshold required to resist dendrite penetration, and meanwhile the high toughness mitigates

fracture-induced failures [49,50]. This directly contributes to the superior cycling stability and high critical current density demonstrated in *section 3.5*.

Additionally, the thermostability of the PL-NS electrolyte was assessed through observation of their shape changes and melting behaviors at various temperatures in ambient condition (Fig. 5e). The pristine PL electrolyte disc soon melted at 60 $^{\circ}$ C, however, only a part of the PL-NS electrolyte discs melted after 2 h at 60 $^{\circ}$ C. Upon elevating the temperature from 60 to 100 $^{\circ}$ C, the PL-NS electrolyte discs still kept their original shape and size, due to the high thermostability of the NSs and the hydrogen bonding between the polymer matrices and the NSs.

3.5. Resistance against Li dendrites of electrolytes

The dendrite suppression capability of the electrolytes was initially evaluated through critical current density (CCD) testing on Li||Li cells at $60\,^{\circ}\text{C}$ (Fig. 6a-d). The cell employing the PL electrolyte showed a low CCD of $0.15\,\text{mA}$ cm $^{-2}$. With the addition of the NSOs, the cell utilizing the PL-NSO1 electrolyte displayed higher CCD of $0.30\,\text{mA}$ cm $^{-2}$. Furtherly, the CCDs of the PL-NSN1 and PL-NSC3 electrolyte-based cells rise to $0.55\,\text{and}~0.65\,\text{mA}~\text{cm}^{-2}$, respectively. Additionally, the Tafel plot

analyses demonstrated that the PL-NSC3 electrolyte-based cell exhibited a much higher exchange current density (1.11×10^{-2} mA cm $^{-2}$) than the PL (5.26×10^{-3} mA cm $^{-2}$), PL-NSO1 (5.88×10^{-3} mA cm $^{-2}$) and PL-NSN1 (7.43×10^{-3} mA cm $^{-2}$) electrolyte-based cells (Fig. 6e). These notable improvements provided strong evidence that the NSC incorporation in the electrolytes not only enhanced the dendrite inhibition ability but also facilitated the Li $^+$ transport kinetics and the electrochemical reactions [47,51].

The stability between the PL-NS electrolyte and lithium electrodes was then assessed through a constant-current measurement on Li||Li cells at 60 °C (Fig. 6f). When cycled under 0.10 mA cm⁻² (areal capacity: 0.10 mAh cm⁻²), the cell employing the PL electrolyte soon short-circuited in 295 h on account of lithium dendrite propagation and penetration in the electrolyte. On the contrary, the PL-NSO1 and PL-NSN1 electrolyte-based Li||Li cells kept stable cycling without short-circuiting for 1215 and 2347 h, respectively. Especially, the cell utilizing the PL-NSC3 electrolyte could stably cycle for 3000 h, again verifying the significantly improved dendrite resistance of the PL-NSC3 electrolyte. The EIS spectra of the cells after the 100 h cycling further showed the less increase of the interfacial resistance of the cell utilizing the PL-NSC3 electrolyte (from 358 to 404 Ω), owing to the improved

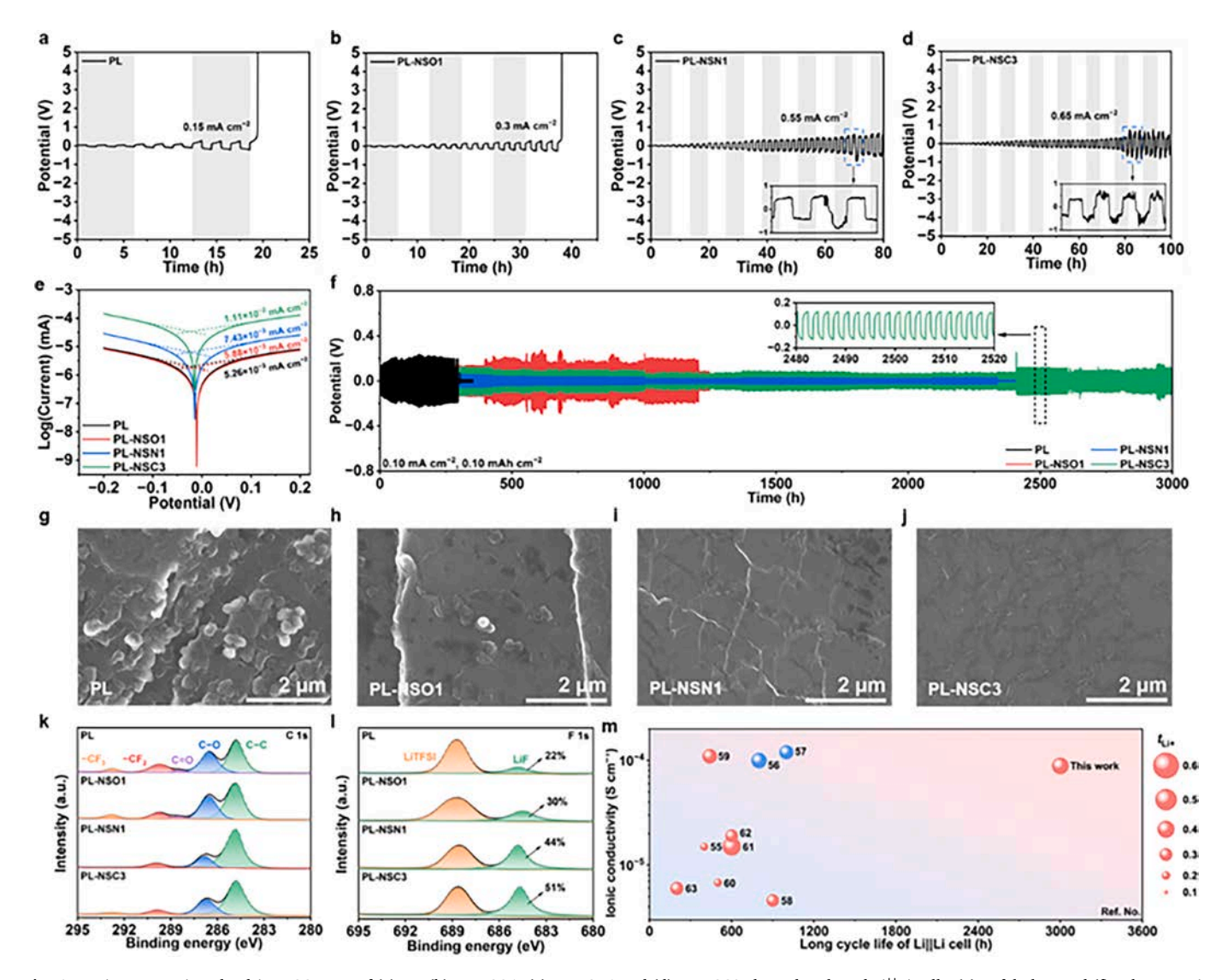


Fig. 6. Resistance against dendrites. CCD test of (a) PL, (b) PL-NSO1, (c) PL-NSN1 and (d) PL-NSC3 electrolyte-based Li||Li cells. (e) Tafel plots and (f) galvanostatic cycling curves of Li||Li cells. SEM images of the surfaces of the cycled Li electrodes paired with (g) PL, (h) PL-NSO1, (i) PL-NSN1 and (j) PL-NSC3 electrolytes. High-resolution (k) C 1s and (l) F 1s XPS spectra of corresponding cycled Li electrodes. Comparison of (m) electrical properties of electrolytes and Li||Li cell performance reported in open literatures [52–60]. More details are given in Table S3.

dendrite resistance and interface stability (Fig. S5).

The corresponding SEM images of the electrochemically cycled Li electrodes from the Li||Li cells were taken to observe the lithium deposition situation (Fig. 6g - j). There are a lot of deposited dendrites on the Li electrodes from the cell employing the PL electrolyte, while the Li electrodes paired with the PL-NSO1 and PL-NSN1 electrolytes have much less lithium dendrites. In particular, the Li electrodes paired with the PL-NSC3 electrolyte are smoother without lithium dendrites, further confirming the higher lithium dendrite inhibition ability of the PL-NSC3 electrolyte and the positive effect of the carboxyl-functionalized NSCs.

The components of solid-state interphase (SEI) on the electrochemically cycled Li electrodes were investigated via XPS. As revealed by the C1 s spectra in Fig. 6k, the intensity of the C-O vibration-related peak at ~ 286.7 eV was weaker in the samples with the PL-NSN1 and PL-NSC3 electrolytes, and the C=O vibration-related peak was absent in the samples with the PL-NSN1 and PL-NSC3 electrolytes, revealing the effective suppression of the generation of carbonate species when using the PL-NSN1 and PL-NSC3 electrolytes [61]. The Li - F peak intensity (at ~ 685.7 eV) area ratios of the Li electrodes paired with the PL-NSN1 (44 %) and PL-NSC3 (51 %) electrolytes was much higher than those of the electrodes paired with the PL (22 %) and PL-NSO1 (30 %) electrolytes (Fig. 61), indicating the formation of LiF-rich SEI layers with the assistance of the NSNs and NSCs. Moreover, there were obvious Li₂S and $\text{Li}_3\text{N-related peaks}$ (at ~ 161.1 and ~ 398.2 eV) on the Li electrodes paired with the PL-NSN1 and PL-NSC3 electrolytes. The peak area ratios of Li₂S and Li₃N were 18 % and 51 % for the Li electrodes paired with the PL-NSN1 electrolyte, and 15 % and 60 % for those paired with the PL-NSC3 electrolyte, respectively (Fig. S6). No peaks related to S_x^{n-} species were detected on the Li electrodes paired with the PL-NSC3 electrolyte [62]. In short, the SEI layers on the Li electrodes paired with the PL-NSC3 electrolyte possessed abundant inorganic components (e.g., LiF, Li2S and Li3N) with high mechanical modulus, surface energy and ionic conductivity [16,63], and thus inhibiting the dendrite propagation for the stable Li||Li battery cycling.

The optimized Li||Li cell performance of the PL-NS electrolyte is

subsequently compared with existing literatures (Fig. 6m and Table S3). The room-temperature ionic conductivity and Li $^+$ transference number of the PL-NSC3 electrolyte demonstrates significant enhancement, compared to those of other PEO-based solid-state electrolytes (Fig. 6m). The Li||Li cell cycle stability at 0.10 mA cm $^{-2}$ (areal capacity: 0.10 mAh cm $^{-2}$) is also higher than the previous reports.

3.6. Lithium metal battery performance

The electrochemical performance of PL-NS composite electrolytes was evaluated in Li||LiFePO₄ cells using galvanostatic cycling tests at 60° C under multiple current densities (Fig. 7a - c and S7). As illustrated in Fig. 7a, the PL-NSC3 electrolyte-based cell demonstrated superior rate capability with much higher capacities of 162, 160, 158, 151 and 92 mAh g⁻¹ than the PL (119, 63, 6, 0 and 0 mAh g⁻¹), PL-NSO1 (148, 144, 138, 120 and 14 mAh g⁻¹) and PL-NSN1 (151, 150, 146, 73 and 0 mAh g⁻¹) electrolyte-based cells at 0.1C to 1.0C respectively, respectively. Upon reverting to 0.1C after 25 cycles, the Li||LiFePO₄ cell utilizing the PL-NSC3 electrolyte maintained a high capacity of 160 mAh g⁻¹, compared to the cells utilizing the PL (105 mAh g⁻¹), PL-NSO1 (147 mAh g⁻¹) and PL-NSN1 (149 mAh g⁻¹) electrolytes. Owing to the high ionic conductivity coupled with a superior $\tau_{\text{Li+}}$ of the PL-NSC3 electrolyte, the cell based on it exhibited small polarization, as evidenced by the voltage plateaus at various C rates (Fig. 7b – c and S7).

The impedance evolution of the Li||LiFePO₄ cells in the pre-cycling and post-cycling states was further measured. (Fig. S8). Compared to the PL (457 and 1228 Ω), PL-NSO1 (213 and 1203 Ω) and PL-NSN1 (382 and 1123 Ω) electrolyte-based Li||LiFePO₄ cells, the PL-NSC3 electrolyte-based Li||LiFePO₄ cell exhibited lower charge transfer resistance (R_{ct}) values (232 and 610 Ω) before and after the cycling of rate performance testing. This was identical with the results in Fig. 6e k – n and S6, again verifying the enhanced charge transfer kinetics by the carboxyl-functionalized NSCs.

The cycling durability of Li||LiFePO $_4$ cells was evaluated at 60 °C (Fig. 7d and S9). The cell utilizing the PL electrolyte exhibited an initial

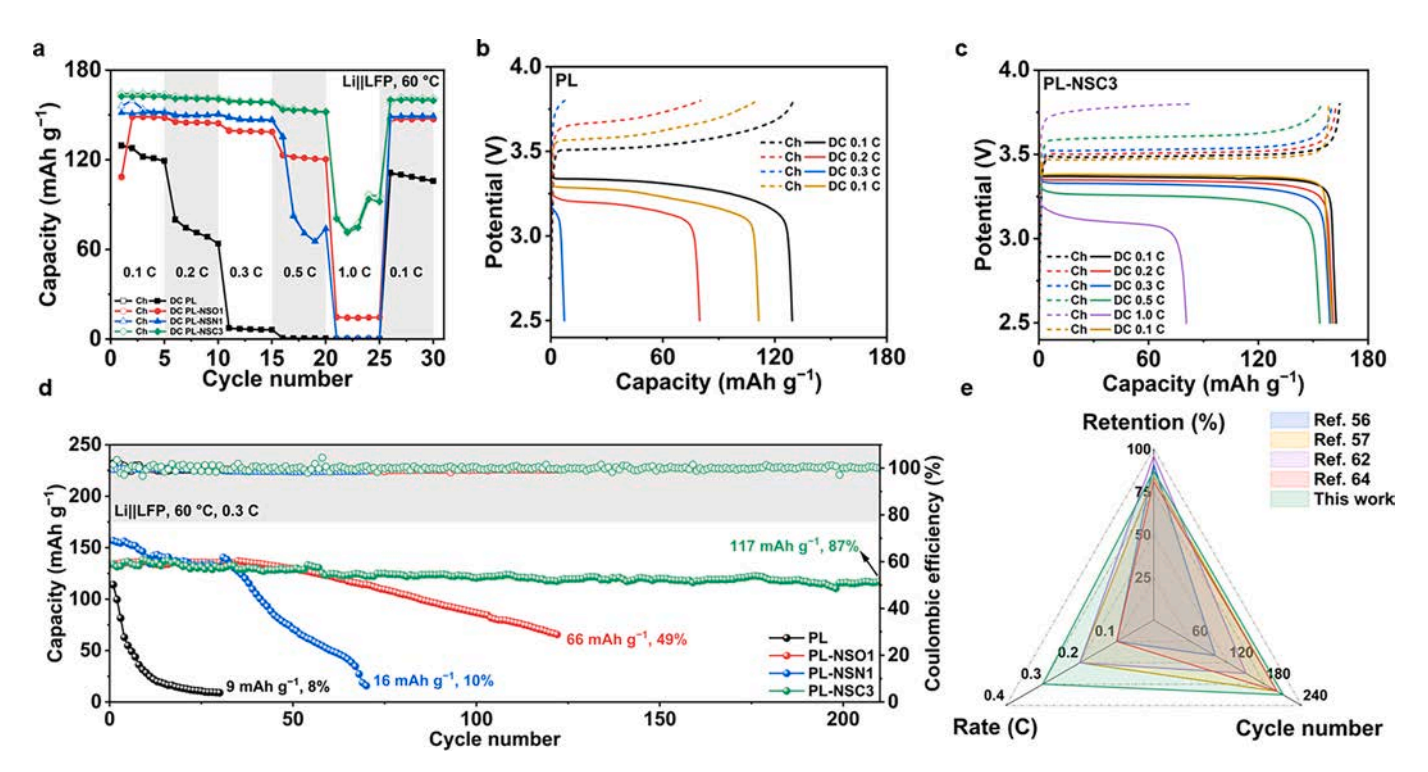


Fig. 7. Lithium metal cell performance. (a) Rate performance of Li||LiFePO₄ cells based on PL, PL-NSO1, PL-NSO1 and PL-NSC3 electrolytes, and the charge–discharge potential profiles of the cells employing (b) PL and (c) PL-NSC3 electrolytes. (d) Cycling performance of Li||LiFePO₄ cells. Comparison of (e) Li||LiFePO₄ cell performance reported in open literatures [53,54,59,64]. More details are given in Table S3.

capacity of 114 mAh g $^{-1}$, but its capacity rapidly declined to 9 mAh g $^{-1}$ within 30 cycles at 0.3 C with a merely 8 % capacity preservation. The capacity retentions increased to 49 % (66 mAh g $^{-1}$, PL-NSO1) and 10 % (16 mAh g $^{-1}$, PL-NSN1) with the incorporation of the NSs in the electrolytes. In comparison, the PL-NSC3 electrolyte-based cell maintained 87 % capacity retention (117 mAh g $^{-1}$) after 210 cycles. Moreover, the charge–discharge potential profiles revealed that the utilization of the PL-NSC3 electrolyte greatly decreased the polarization (Fig. S9).

The optimized Li||LiFePO₄ cell performance of the PL-NS electrolyte is subsequently compared with existing literature (Fig. 7e and Table S3). Notably, compared to the previous reports, the PL-NSC3 electrolyte-based Li||LiFePO₄ cells exhibit superior performance (Fig. 7f).

4. Conclusions

In summary, porous silica NSs with hydroxy, amino or carboxyl groups were incorporated to boost the comprehensive properties of PL electrolytes, and the role of the functional groups of the NSs was disclosed. Because of the hydrogen bonding between the functional groups and the ether oxygen groups of PEO and the TFSI⁻ anions of LiTFSI, the functionalized NSs effectively suppressed the PEO crystallization and facilitated the LiTFSI decomposition, thus resulting in the significant enhancement in ionic conductivity (8.9 \times 10⁻⁵ vs. 7.5 \times 10⁻⁶ S cm⁻¹ at 30 °C), mechanical toughness (1.47 vs. 0.24 MJ m⁻³), thermal stability and oxidization stabilization potential (5.15 vs. 3.95 V). Moreover, the incorporation of the functionalized NSs effectively inhibited the lithium dendrite growth with the CCD increase from 0.15 to 0.65 mA cm⁻² and the Li||Li cell cycling life increase from 295 to 3000 h. The NS-modified electrolyte-based Li||LiFePO4 cells also displayed superior rate performance than the cells employing the PL electrolytes, and delivered 87 % capacity retention at 0.3 C after 210 cycles. This work offered a facile road to realize comprehensively-updated electrolytes by constructing hydrogen bond networks for high-performance LMBs.

CRediT authorship contribution statement

Lehao Liu: Writing – review & editing, Writing – original draft, Visualization, Validation, Supervision, Software, Resources, Project administration, Methodology, Investigation, Funding acquisition, Formal analysis, Data curation, Conceptualization. Tianrong Yang: Visualization, Validation, Supervision, Software, Methodology, Investigation, Formal analysis, Data curation. Rubing Xu: Visualization, Validation, Supervision, Software, Methodology, Investigation, Formal analysis, Data curation. Dingrong Long: Software, Formal analysis, Data curation. Jiaxin Tu: Software, Formal analysis, Data curation. Rongmin Zhou: Software, Formal analysis, Data curation. Qian Zhao: Software, Formal analysis, Data curation. Weicheng Li: Writing – review & editing, Writing – original draft, Visualization, Validation, Supervision, Software, Resources, Project administration, Methodology, Investigation, Funding acquisition, Formal analysis, Data curation, Conceptualization.

Declaration of competing interest

The authors declare that they have no known competing financial interests or personal relationships that could have appeared to influence the work reported in this paper.

Acknowledgments

This work is supported partially by project of National Natural Science Foundation of China (52272200, 52302250), Hebei Natural Science Foundation (E2022502022), the project of China Three Gorges Corporation named key technologies of intelligent joint regulation and operation with grid connected friendly in power station group of wind, solar photovoltaic and energy storage (WWKY-2021-0173), Huaneng

Group Headquarters Science and Technology Project (HNKJ20-H88), the Fundamental Research Funds for the Central Universities (2025MS040), and the NCEPU "Double First-Class" Program.

Appendix A. Supplementary data

Supplementary data to this article can be found online at https://doi.org/10.1016/j.apsusc.2025.164825.

Data availability

Data will be made available on request.

References

- L. Liu, M. Li, L. Chu, B. Jiang, R. Lin, X. Zhu, G. Cao, Layered ternary metal oxides: Performance degradation mechanisms as cathodes, and design strategies for highperformance batteries, Prog. Mater Sci. 111 (2020) 100655.
- [2] M. Xu, S. Liang, H. Shi, J. Miao, F. Tian, W. Cui, R. Shao, Z. Xu, High-strength MOF-based polymer electrolytes with uniform ionic flow for lithium dendrite suppression, Small 20 (2024) 2406007.
- [3] D. Zhang, X. Meng, W. Zhang, J. Mo, Q. Zhao, B. Wang, Q. Fan, L. Liu, T. Yang, Y. Jin, R. Zhou, M. Zhang, M. Li, A thin and ultrahigh-ionic-conductivity composite electrolyte with 3D aramid nanofiber networks toward ambient-temperature lithium metal batteries, Adv. Energy Mater. 15 (2025) 2403565.
- [4] L. Liu, D. Zhang, T. Yang, W. Hu, X. Meng, J. Mo, W. Hou, Q. Fan, K. Liu, B. Jiang, L. Chu, M. Li, Flexible ion-conducting membranes with 3D continuous nanohybrid networks for high-performance solid-state metallic lithium batteries, Journal of Energy Chemistry 75 (2022) 360–368.
- [5] X. Liu, H. Jia, H. Li, Flame-retarding quasi-solid polymer electrolytes for high-safety lithium metal batteries, Energy Storage Mater. 67 (2024) 103263.
- [6] K. Chen, J. Liu, X. Zhang, Y. Sun, H. Xie, Three-dimensional cross-linked network deep eutectic gel polymer electrolyte with the self-healing ability enable by hydrogen bonds and dynamic disulfide bonds, J. Colloid Interface Sci. 669 (2024) 529–536.
- [7] J. Guo, H. Xu, Y. Sun, K. Chen, X. Zhang, H. Xie, Y. Jiang, J. Liu, Borate-containing triblock copolymer electrolytes for improved lithium-ion transference number and interface stability, J. Colloid Interface Sci. 660 (2024) 565–573.
- [8] D. Zhang, X. Meng, W. Hou, W. Hu, J. Mo, T. Yang, W. Zhang, Q. Fan, L. Liu, B. Jiang, L. Chu, M. Li, Solid polymer electrolytes: Ion conduction mechanisms and enhancement strategies, Nano Research Energy 2 (2023) e9120050.
- [9] Y. Jiang, K. Chen, J. He, Y. Sun, X. Zhang, X. Yang, H. Xie, J. Liu, A self-healing composite solid electrolyte with dynamic three-dimensional inorganic/organic hybrid network for flexible all-solid-state lithium metal batteries, J. Colloid Interface Sci. 678 (2025) 200–209.
- [10] J. Cheng, Y. Zhang, H. Chao, Y. Huang, H. Qin, L. Cao, X. Teng, H. Hu, M. Wu, High performance lithium-ion capacitors based on dynamic matching principle, J. Mater. Eng. 51 (2023) 29–37.
- [11] H. An, M. Li, Q. Liu, Y. Song, J. Liu, Z. Yu, X. Liu, B. Deng, J. Wang, Strong Lewisacid coordinated PEO electrolyte achieves 4.8 V-class all-solid-state batteries over 580 Wh kg⁻¹, Nat. Commun. 15 (2024) 9150.
- [12] W. Liu, J. Liu, Z. Yang, M. Liu, S. Sang, H. Liu, Flaky Li-doped high-entropy oxide enables PEO-based composite solid electrolyte with extended suitability for lithium metal batteries, Adv. Funct. Mater. 2419095 (2024).
- [13] L. Liu, J. Mo, R. Zhou, T. Yang, R. Xu, J. Tu, Q. Zhao, M. Zhang, D. Zhang, B. Wang, D. Long, K. Yang, J. Zhang, M. Li, Ultrathin solid composite electrolytes for long-life lithium metal batteries, J. Storage Mater. 114 (2025) 115777.
- [14] K. Khan, M.B. Hanif, H. Xin, A. Hussain, H.G. Ali, B. Fu, Z. Fang, M. Motola, Z. Xu, M. Wu, PEO-based solid composite polymer electrolyte for high capacity retention all-solid-state lithium metal battery, Small 20 (2024) 2305772.
- [15] L. Liu, R. Xu, J. Tu, R. Zhou, J. Mo, T. Yang, Q. Zhao, M. Zhang, D. Zhang, M. Li, Thin Polymer Electrolytes with 3D Nanofiber Skeletons Enabling High-Performance Solid-State Lithium Metal Batteries, J. Phys. Chem. C 129 (2025) 6138–6147.
- [16] X. Da, J. Chen, Y. Qin, J. Zhao, X. Jia, Y. Zhao, X. Deng, Y. Li, N. Gao, Y. Su, Q. Rong, X. Kong, J. Xiong, X. Hu, S. Ding, G. Gao, CO₂-assisted induced self-assembled aramid nanofiber aerogel composite solid polymer electrolyte for all-solid-state lithium-metal batteries, Adv. Energy Mater. 14 (2024) 2303527.
- [17] L. Zhao, Q. Dong, Y. Wang, G. Xue, X. Wang, Z. Li, H. Shao, H. Chen, Y. Shen, L. Chen, Anion modulation: Enabling highly conductive stable polymer electrolytes for solid-state Li-metal batteries, Angew. Chem. Int. Ed. 63 (2024) e202412280.
- [18] X. Guan, Y. Li, X. Liu, Research progress in stabilization of interface and bulk structure of lithium metal anodes, J. Mater. Eng. 52 (2024) 1–14.
- 19] L. Liu, J. Lyu, J. Mo, H. Yan, L. Xu, P. Peng, J. Li, B. Jiang, L. Chu, M. Li, Comprehensively-upgraded polymer electrolytes by multifunctional aramid nanofibers for stable all-solid-state Li-ion batteries, Nano Energy 69 (2020) 104398.
- [20] X. Yang, J. Liu, N. Pei, Z. Chen, R. Li, L. Fu, P. Zhang, J. Zhao, The critical role of fillers in composite polymer electrolytes for lithium battery, Nano-Micro Letters 15 (2023) 74.
- [21] Z. Hong, P. Li, Q. Zou, L. Gu, J. Wang, L. Deng, C. Wang, Y. Zhang, M. Li, J. Chen, R. Si, C. Yang, Metal organic framework (MOF-808) incorporated composite

- polymer electrolyte for stable all-solid-state lithium batteries, ACS Appl. Energy Mater. 7 (2024) 11967–11976.
- [22] N. Meng, Y. Ye, Z. Yang, H. Li, F. Lian, Developing single-ion conductive polymer electrolytes for high-energy-density solid state batteries, Adv. Funct. Mater. 33 (2023) 2305072.
- [23] H. Zhang, C. Li, M. Piszcz, E. Coya, T. Rojo, L.M. Rodriguez-Martinez, M. Armand, Z. Zhou, Single lithium-ion conducting solid polymer electrolytes: advances and perspectives, Chem. Soc. Rev. 46 (2017) 797–815.
- [24] Y. Cheng, Z. Cai, J. Xu, Z. Sun, X. Wu, J. Han, Y.-H. Wang, M.-S. Wang, Zwitterionic cellulose-based polymer electrolyte enabled by aqueous solution casting for highperformance solid-state batteries, Angew. Chem. Int. Ed. 63 (2024) e202400477.
- [25] X. Meng, D. Zhang, J. Mo, L. Liu, T. Yang, Q. Fan, Q. Zhao, R. Zhou, M. Zhang, W. Hou, W. Hu, W. Zhang, Y. Jin, B. Jiang, L. Chu, M. Li, Room-temperature solid-state metallic lithium batteries based on high-content boron nitride nanosheet-modified polymer electrolytes, Appl. Surf. Sci. 648 (2024) 158962.
- [26] P. Zhai, N. Peng, Z. Sun, W. Wu, W. Kou, G. Cui, K. Zhao, J. Wang, Thin laminar composite solid electrolyte with high ionic conductivity and mechanical strength towards advanced all-solid-state lithium-sulfur battery, J. Mater. Chem. A 8 (2020) 23344-23353
- [27] W.-Y. Li, Z.-H. Luo, X. Long, J.-Y. Long, C. Pang, H. Li, X. Zhi, B. Shi, J.-J. Shao, Y.-B. He, Cation vacancy-boosted Lewis acid-base interactions in a polymer electrolyte for high-performance lithium metal batteries, ACS Appl. Mater. Interfaces 13 (2021) 51107–51116.
- [28] F. Pei, Y. Huang, L. Wu, S. Zhou, Q. Kang, W. Lin, Y. Liao, Y. Zhang, K. Huang, Y. Shen, L. Yuan, S.-G. Sun, Z. Li, Y. Huang, Multisite crosslinked poly(ether-urethane)-based polymer electrolytes for high-voltage solid-state lithium metal batteries, Adv. Mater. 36 (2024) 2409269.
- [29] L. Wang, X. Wang, J. Yin, C. Wang, Insights into the physicochemical characteristics from vermiculite to silica nanosheets, Appl. Clay Sci. 132–133 (2016) 17–23.
- [30] Z. Luo, W. Li, C. Guo, Y. Song, M. Zhou, Y. Shi, J. Xu, L. Li, B. Shi, Q. Ouyang, J.-J. Shao, G. Zhou, Two-dimensional silica enhanced solid polymer electrolyte for lithium metal batteries, Particuology 85 (2024) 146–154.
- [31] X. Li, R. Li, K. Peng, L. Fu, K. Zhao, H. Li, J. Peng, L. Wang, Interlayer functionalization of vermiculite derived silica with hierarchical layered porous structure for stable CO₂ adsorption, Chem. Eng. J. 435 (2022) 134875.
- [32] R.C. Puerari, E. Ferrari, M.G. de Cezar, R.A. Gonçalves, C. Simioni, L.C. Ouriques, D.S. Vicentini, W.G. Matias, Investigation of toxicological effects of amorphous silica nanostructures with amine-functionalized surfaces on Vero cells, Chemosphere 214 (2019) 679–687.
- [33] S.S.G. Santos, H.R.M. Silva, A.G. de Souza, A.P.M. Alves, E.C. da Silva Filho, M. G. Fonseca, Acid-leached mixed vermiculites obtained by treatment with nitric acid, Appl. Clay Sci. 104 (2015) 286–294.
- [34] M. Ritz, J. Zdrálková, M. Valášková, Vibrational spectroscopy of acid treated vermiculites, Vib. Spectrosc 70 (2014) 63–69.
- [35] J. Madejová, M. Pentrák, H. Pálková, P. Komadel, Near-infrared spectroscopy: a powerful tool in studies of acid-treated clay minerals, Vib. Spectrosc 49 (2009) 211–218.
- [36] Y. Joo, Y. Jeon, S.U. Lee, J.H. Sim, J. Ryu, S. Lee, H. Lee, D. Sohn, Aggregation and stabilization of carboxylic acid functionalized halloysite nanotubes (HNT-COOH), J. Phys. Chem. C 116 (2012) 18230–18235.
- [37] Q. He, D. Yang, X. Deng, Q. Wu, R. Li, Y. Zhai, L. Zhang, Preparation, characterization and application of N-2-Pyridylsuccinamic acid-functionalized halloysite nanotubes for solid-phase extraction of Pb(II), Water Res. 47 (2013) 3976–3983
- [38] S.S. Zargarian, V. Haddadi-Asl, H. Hematpour, Carboxylic acid functionalization of halloysite nanotubes for sustained release of diphenhydramine hydrochloride, J. Nanopart. Res. 17 (2015) 218.
- [39] M. Liu, Y. Chang, J. Yang, Y. You, R. He, T. Chen, C. Zhou, Functionalized halloysite nanotube by chitosan grafting for drug delivery of curcumin to achieve enhanced anticancer efficacy, J. Mater. Chem. B 4 (2016) 2253–2263.
- [40] X. Zhang, G. Wu, Grafting halloysite nanotubes with amino or carboxyl groups onto carbon fiber surface for excellent interfacial properties of silicone resin composites, Polymers 10 (2018) 1171.
- [41] L. Yang, C. Fan, J. Zhang, F. Zhang, R. Li, S. Yi, Y. Sun, H. Dong, Poly(acrylic acid)-modified silica nanoparticles as a nonmetal catalyst for NaBH₄ methanolysis, Int. J. Hydrogen Energy 46 (2021) 23236–23244.
- [42] M. Xie, K. Huang, F. Yang, R. Wang, L. Han, H. Yu, Z. Ye, F. Wu, Chitosan nanocomposite films based on halloysite nanotubes modification for potential biomedical applications, Int. J. Biol. Macromol. 151 (2020) 1116–1125.

- [43] Z. Wang, L. Ouyang, H. Li, L. Wågberg, M.M. Hamedi, Layer-by-layer assembly of strong thin films with high lithium ion conductance for batteries and beyond, Small 17 (2021) 2100954.
- [44] Z. Zou, Y. Li, Z. Lu, D. Wang, Y. Cui, B. Guo, Y. Li, X. Liang, J. Feng, H. Li, C.-W. Nan, M. Armand, L. Chen, K. Xu, S. Shi, Mobile ions in composite solids, Chem. Rev. 120 (2020) 4169–4221.
- [45] Q. Wang, J.-F. Wu, Z.-Y. Yu, X. Guo, Composite polymer electrolytes reinforced by two-dimensional layer-double-hydroxide nanosheets for dendrite-free lithium batteries, Solid State Ion. 347 (2020) 115275.
- [46] B.-Y. Chi, K. Wang, X.-J. Gao, K.-H. Wang, W.-F. Ren, R.-C. Sun, Carboxymethyl chitosan composited poly(ethylene oxide) electrolyte with high ion conductivity and interfacial stability for lithium metal batteries, Int. J. Biol. Macromol. 273 (2024) 132993.
- [47] K. Liu, H. Cheng, Z. Wang, Y. Zhao, Y. Lv, L. Shi, X. Cai, Z. Cheng, H. Zhang, S. Yuan, A 3 µm-utrathin hybrid electrolyte membrane with integrative architecture for all-solid-state lithium metal batteries, Adv. Energy Mater. 2303940 (2024).
- [48] Z. Yang, Z. Zhang, Y. Liu, Y. Fang, C. Li, X. Cao, Enhancement mechanism of the comprehensive performance of all-solid-state polymer electrolytes by halloysite nanotubes: Construction of efficient lithium-ion conduction channels, J. Power Sources 603 (2024) 234391.
- [49] C. Monroe, J. Newman, The impact of elastic deformation on deposition kinetics at lithium/polymer interfaces, J. Electrochem. Soc. 152 (2005) A396.
- [50] C. Monroe, J. Newman, The effect of interfacial deformation on electrodeposition kinetics, J. Electrochem. Soc. 151 (2004) A880.
- [51] C. He, H. Ying, L. Cai, H. Chen, Z. Xu, S. Liu, P. Huang, H. Zhang, W. Song, J. Zhang, L. Shi, W. Gao, D. Li, W.-Q. Han, Tailoring stable PEO-based electrolyte/ electrodes interfaces via molecular coordination regulating enables 4.5 V solidstate lithium metal batteries, Adv. Funct. Mater. 34 (2024) 2410350.
- [52] E. Zhao, Y. Guo, Y. Liu, S. Liu, G. Xu, Nanostructured zeolitic imidazolate framework-67 reinforced poly(ethylene oxide) composite electrolytes for all solid state Lithium ion batteries, Appl. Surf. Sci. 573 (2022) 151489.
- [53] C. Li, Y. Huang, C. Chen, X. Feng, Z. Zhang, High-performance polymer electrolyte membrane modified with isocyanate-grafted Ti³⁺ doped TiO₂ nanowires for lithium batteries, Appl. Surf. Sci. 563 (2021) 150248.
- [54] C. Li, Y. Huang, X. Feng, Z. Zhang, H. Gao, J. Huang, Silica-assisted cross-linked polymer electrolyte membrane with high electrochemical stability for lithium-ion batteries, J. Colloid Interface Sci. 594 (2021) 1–8.
- [55] Y. Li, Y. Qin, J. Zhao, M. Ma, M. Zhang, P. Li, S. Lu, H. Bu, K. Xi, Y. Su, S. Ding, Boosting the ion mobility in solid polymer electrolytes using hollow polymer nanospheres as an additive, ACS Appl. Mater. Interfaces 14 (2022) 18360–18372.
- [56] Q. Guo, F. Xu, L. Shen, Z. Wang, J. Wang, H. He, X. Yao, Poly(ethylene glycol) brush on Li_{6.4}La₃Zr_{1.4}Ta_{0.6}O₁₂ towards intimate interfacial compatibility in composite polymer electrolyte for flexible all-solid-state lithium metal batteries, J. Power Sources 498 (2021) 229934.
- [57] E. Zhao, Y. Guo, A. Zhang, H. Wang, G. Xu, Polydopamine coated TiO₂ nanofiber fillers for polyethylene oxide hybrid electrolytes for efficient and durable all solid state lithium ion batteries, Nanoscale 14 (2022) 890–897.
- [58] J. Wen, Q. Zhao, X. Jiang, G. Ji, R. Wang, G. Lu, J. Long, N. Hu, C. Xu, Graphene oxide enabled flexible Peo-based solid polymer electrolyte for all-solid-state lithium metal battery, ACS Appl. Energy Mater. 4 (2021) 3660–3669.
- [59] C. Li, Y. Huang, C. Chen, X. Feng, Z. Zhang, P. Liu, A high-performance solid electrolyte assisted with hybrid biomaterials for lithium metal batteries, J. Colloid Interface Sci. 608 (2022) 313–321.
- [60] X. Yin, L. Wang, Y. Kim, N. Ding, J. Kong, D. Safanama, Y. Zheng, J. Xu, D.V. M. Repaka, K. Hippalgaonkar, S.W. Lee, S. Adams, G.W. Zheng, Thermal Conductive 2D Boron Nitride for High-Performance All-Solid-State Lithium—Sulfur Batteries. Adv. Sci. 7 (2020) 2001303.
- [61] M. Yao, Q. Ruan, S. Pan, H. Zhang, S. Zhang, An ultrathin asymmetric solid polymer electrolyte with intensified ion transport regulated by biomimetic channels enabling wide-temperature high-voltage lithium-metal battery, Adv. Energy Mater. 13 (2023) 2203640.
- [62] Y. Wei, T.-H. Liu, W. Zhou, H. Cheng, X. Liu, J. Kong, Y. Shen, H. Xu, Y. Huang, Enabling all-solid-state Li metal batteries operated at 30 °C by molecular regulation of polymer electrolyte, Adv. Energy Mater. 13 (2023) 2203547.
- [63] T. Li, X.-Q. Zhang, P. Shi, Q. Zhang, Fluorinated solid-electrolyte interphase in high-voltage lithium metal batteries, Joule 3 (2019) 2647–2661.
- [64] J. Cheng, G. Hou, Q. Chen, D. Li, K. Li, Q. Yuan, J. Wang, L. Ci, Sheet-like garnet structure design for upgrading PEO-based electrolyte, Chem. Eng. J. 429 (2022) 132343.